

Magnetorotational core collapse of possible GRB progenitors. IV. A wider range of progenitors

M. Obergaulinger^{1,2}, M.Á. Aloy^{1,3}

¹ Departament d’Astronomia i Astrofísica, Universitat de València, C/ Dr. Moliner, 50, 46100 Burjassot, Spain

² Institut für Kernphysik, Technische Universität Darmstadt, Schlossgartenstraße 2, 64289 Darmstadt, Germany

³ Observatori Astronòmic, Universitat de València, 46980 Paterna, Spain

21 June 2022

ABSTRACT

The final collapse of the cores of massive stars can lead to a wide variety of outcomes in terms of electromagnetic and kinetic energies, nucleosynthesis, and remnants. While the connection of this wide spectrum of explosion and remnant types to the properties of the progenitors remains an open issue, rotation and magnetic fields in Wolf-Rayet stars of subsolar metallicity have been suggested as explanations for extreme events such as superluminous supernovae and gamma-ray bursts powered by proto-magnetars or collapsars. Continuing numerical studies of magnetorotational core collapse including detailed neutrino physics, we focus on progenitors with zero-age main-sequence masses in the range between 5 and 39 solar masses. All of the pre-collapse stars were calculated in spherical symmetry employing prescriptions for the effects of rotation and magnetic fields, with eight of the ten stars we consider being the results of chemically homogeneous evolution due to enhanced rotational mixing (Aguilera-Dena et al. 2018). All but one of them produce explosions driven by neutrino heating (more likely for low mass progenitors up to 8 solar masses) and non-spherical flows or by magnetorotational stresses (more frequent above 26 solar masses). In most of them and for the one non-exploding model, ongoing accretion leads to black-hole formation. Rapid rotation makes a subsequent collapsar activity plausible. If no black hole is formed, proto-magnetar driven jets can be expected and are, in fact, found in the simulations. Conditions for the formation of nickel are more favourable in magnetorotationally driven models, though our rough estimates fall short of the requirements for extremely bright events.

Key words: Supernovae: general - gamma-ray bursts: general - stars: neutron - stars: black holes - (*magnetohydrodynamics*) MHD

1 INTRODUCTION

The collapse of the core of a star of more than about $8 M_{\odot}$ after the end of its hydrostatic burning phases initiates a sequence of processes leading to one of several quite different outcomes that range from the formation of a black hole (BH) devouring the entire star to various classes of core-collapse supernovae (CCSNe) and long gamma-ray bursts (GRBs). These explosions are ultimately powered by the gravitational binding energy liberated during the collapse and the subsequent accretion of matter onto the core. While this energy source is universal, there are different mechanisms for converting a fraction of it to the kinetic and internal energy of the ejecta of the explosion. Hence, the evolution depends on the pre-collapse state of the progenitor star and on a multitude of complex, interconnected processes occurring during and after the collapse and the birth of a proto-neutron star (PNS).

The detection of neutrinos from supernova SN 1987A, a large number of increasingly detailed multi-dimensional simulations, and the comparison of their results to electromagnetic observations of CCSNe and young supernova remnants (SNRs) offer confirmation for the standard neutrino-driven mechanism (for a review, see Janka 2012). This scenario, based on neutrinos depositing energy and on non-radial fluid instabilities in the hot bubble surrounding the PNS, is able to explain the bulk of the observed CCSNe without requiring special conditions for the progenitor.

However, it remains difficult to account for the most extreme events such as hypernovae (HNe; Iwamoto et al. 1998), i.e., the most energetic class of CCSNe, or long GRBs characterized by collimated, relativistic outflows. Since these events constitute only a minor fraction of the entire population, they have been connected to special progenitor classes, in particular stars with high rotation rates. In these cases,

magnetic fields may play a crucial role in launching the explosion by tapping into the rotational energy. Additionally, rotation and magnetic fields have been invoked to explain the extraordinary brightness of super-luminous supernovae (SLSNe; e.g. Gal-Yam 2012; Moriya et al. 2018; Inserra 2019).

The basic building blocks of magnetorotational models are either a fast spinning, strongly magnetized PNS, a so-called proto-magnetar (PM; Kasen & Bildsten 2010; Woosley 2010; Metzger et al. 2011; Nicholl et al. 2017), whose spin-down drives the explosion (HNe or GRBs) or heats the ejecta (SLSNe), or accretion of rapidly rotating matter onto a BH magnetically powering relativistic jets (collapsar model for GRBs; MacFadyen et al. 2001; Obergaulinger & Aloy 2017).

Whether the strong magnetic fields required for these types of explosions can be reached depends on various processes amplifying them in the collapsed core and on the pre-collapse configuration. Therefore, models for this class of explosions should be based on progenitor stars that include the effects of rotation and magnetic fields in a self-consistent manner. However, the computational costs for covering the entire pre-collapse life of a star up to collapse restrict stellar evolution calculations to the assumption of spherical symmetry, thus allowing for an inclusion of these effects only in approximate ways. Among the most advanced such approximations is the model for a dynamo in convectively stable layers of stars proposed by Spruit (2002) which has been incorporated into spherically symmetric stellar evolution models to produce pre-collapse models (e.g., Heger et al. 2005). Woosley & Heger (2006) presented a set of potential progenitors for GRBs that have found wide application in numerical investigations of stellar core collapse and its aftermath. Among those studies, we refer to the previous articles in this series (Obergaulinger & Aloy 2020; Aloy & Obergaulinger 2021; Obergaulinger & Aloy 2021) evolving various variations of two progenitors in axisymmetry as well as three dimensions including all the physics relevant during the formation of the PNS and the subsequent evolution until explosion (or lack thereof). We note that many other works took a different approach and simulated the propagation of relativistic jets in progenitors of this group under the assumption that the cores develop the conditions necessary for producing a GRB (for an overview, see, e.g., Corsi & Lazzati 2021).

More recently, Aguilera-Dena et al. (2018) (AD18) as well as Aguilera-Dena et al. (2020) have produced a sequence of rotating, magnetized pre-collapse models for Wolf-Rayet stars marked by strong stellar winds. The resulting loss of the outer layers is, besides rotation and magnetic fields, another important ingredient in models for the aforementioned extreme explosions. It is, however, accompanied by a loss of angular momentum, which might reduce the prospects of retaining enough rotational energy for such an explosion. Nevertheless, an adjustment of the mixing of gas between different layers induced by rotation caused the stars to evolve in a chemically homogeneous way and end their lives with high angular velocities. AD18 used an approximation to predict the possible outcome of the core collapse of their models, finding several candidates for SLSNe and for GRBs driven by PMs and collapsars.

As the studies on magnetorotational core collapse sum-

marized above indicate, the models of AD18 in principle possess the right properties to produce SLSNe and GRBs. Thus, a closer investigation by self-consistent simulations of the collapse and the subsequent phases is needed, and this is the motivation of this paper. We combine magnetohydrodynamics (MHD) and a two-moment neutrino transport to follow the evolution of eight of their progenitor models between 5 and $39 M_{\odot}$. Our goal is to check the predictions regarding the evolution of the stars. To this end, long simulation times and a large number of models are required. For this reason, we restrict ourselves at this point to two-dimensional models and defer detailed three-dimensional models to a later stage.

This article is organized as follows: Sect. 2 briefly introduces the physics included in the simulations and the numerical methods, Sect. 3 summarizes the progenitor models selected in this study, Sect. 4 presents the simulation results, Sect. 5 roughly estimates the observable signal of the models, and Sect. 6 ends the article with concluding remarks.

2 INPUT PHYSICS AND NUMERICS

Methodologically, the present study follows our previous work on stellar core collapse (Obergaulinger et al. 2014; Obergaulinger & Aloy 2017, 2020). We employed the simulation code Alcar (Just et al. 2015) for solving the combined systems of equations of special relativistic MHD equations and spectral two-moment neutrino transport. The gas is described by the SFHo equation of state (EOS) of Steiner et al. (2013) applied at densities $\rho > \rho_{\text{EOS}} = 6000 \text{ g cm}^{-3}$ and an EOS accounting for a mixture of photons, electrons and positrons, and nucleons below this threshold. The nuclear composition is determined from nuclear statistical equilibrium (NSE) and using the flashing scheme of Rampp & Janka (2002) in the high-density and low-density regimes, respectively. The self-gravity of the gas is modelled by version 'A' of the TOV potential of Marek et al. (2006), which yields a very close approximation to general relativity in terms of, e.g., the evolution of the density profiles of PNSs and the maximum mass of stable cold neutron stars.

We evolve neutrinos in the two-moment transport scheme consisting of a set of balance equations for their energy (0th moment) and momentum (1st moment) densities closed by a local algebraic expression for the pressure tensor (2nd moment). One pair of these equations is solved for each neutrino species (electron neutrinos, electron anti-neutrinos, and heavy-lepton neutrinos) and for each one of several bins in the space of neutrino energies. The energy bins are coupled by velocity-dependent and gravitational terms in the $\mathcal{O}(v/c)$ -plus method of Endeve et al. (2012). Neutrinos and matter interact via the most important reactions: nucleonic and nuclear absorption, emission, and scattering, inelastic scattering off electrons, and the pair processes of electron-positron annihilation and nucleonic bremsstrahlung.

The simulations are run in spherical coordinates assuming axisymmetry. We set up grids with $n_r = 480$ radial zones distributed logarithmically up to an outer radius of $R_{\text{out}} = 7 \times 10^{10} \text{ cm}$ and $n_{\theta} = 128$ zones in angle. In energy, a logarithmic grid of $n_{\epsilon} = 10$ bins with a maximum energy of $\epsilon_{\text{max}} = 240 \text{ MeV}$ is used.

3 INITIAL MODELS

Our set of models includes a progenitor employed in our previous studies, viz. a star of an initial mass of $M_{\text{ZAMS}} = 35 M_{\odot}$ and sub-solar metallicity ($Z = 0.1 Z_{\odot}$) evolved to the pre-collapse stage with rotation and magnetic fields by Woosley & Heger (2006). Among the different versions of the models based on the progenitor 350C, we only use the one with profiles of rotation and magnetic field taken from the stellar evolution calculations as a comparison model here. The model was named 350C-R0 in the previous articles of this series; for the sake of brevity, we refer to it as model 350C in the following.

From the same source, we add the progenitor star 16TI to our sample. This star has an initial mass of $M_{\text{ZAMS}} = 16 M_{\odot}$ and the same metallicity as model 350C. Considered a plausible collapsar progenitor due to its structure and in particular its fast rotation, it has been used in several studies of the propagation of jets launched by an BH-accretion-disc system through the stellar envelope. However, previous work such as that of, e.g., Lazzati et al. (2009); Lazzati et al. (2012); Hayakawa & Maeda (2018); Aloy et al. (2018), are based on the assumption that the core has formed such a configuration. The central regions, including the BH-torus system or any other type of compact remnant, are excised and a jet injected through suitably chosen inner boundary is evolved in the framework of relativistic (magneto-)hydrodynamics. By simulating the phase prior to that stage, we complement these studies and explore the possibility of this star actually satisfying the conditions for launching a collapsar jet in the first place.

All the other initial conditions of our simulations are given by eight stellar models computed by AD18. These are models for rapidly rotating Wolf-Rayet stars with magnetic fields at subsolar metallicity of $Z = 0.02 Z_{\odot}$ evolved in spherical symmetry using the Modules for Experiments in Stellar Astrophysics (MESA) code (Paxton et al. 2011, 2013, 2015, 2018). The magnetic fields are evolved following the Taylor-Spruit dynamo (Heger et al. 2005), i.e., the treatment of magnetic fields through the stellar evolution is effectively the same as in models 350C and 16TI. The stars are set up with an angular velocity rate close to the critical rotation rate. The fast rotation leads to efficient mixing across different layers of the star. Thereby, these models undergo a chemically homogeneous evolution (CHE). AD18 computed two sets of models, one with the standard sets of parameters and another one with an increased rate of rotational mixing (series B). It is from the latter that we select our pre-collapse models.

At the end of their hydrostatic evolution, the stars of series B have lost their H envelope and most of the He layer. They retain a large amount of angular momentum and possess magnetic fields whose strength depends on the specific progenitor. These properties make them possible progenitors for type Ic SLSNe or GRBs. AD18 explored the types of explosions to be expected as follows:

- The stars with lowest initial masses ($M_{\text{ZAMS}} = 5, 8$, and $13 M_{\odot}$) may explode as type Ic SLSNe in which the excess luminosities are caused mostly by energy input from a central PM.
- The stars with higher masses fulfil the expectations for forming a GRB, in particular in terms of the angular mo-

mentum in the core. AD18 suggest that the ones in an intermediate mass range (models with 17 and $20 M_{\odot}$) might avoid BH formation and thus yield to PM-powered GRBs.

- More massive stars (in our sample, the ones with $26, 30$, and $39 M_{\odot}$) might end their lives as collapsars.
- Though we do not include them in our sample, we note for the sake of completeness that AD18 also consider more massive stars that might, after undergoing pulsational pair instability, explode as GRBs or HNe and, by interaction with the stellar winds evolve into SLSNe.

In the process of mapping the stellar models at the onset of collapse onto our 2d grid, we have to convert the radial profiles of the poloidal and toroidal field components into the three vector components of the magnetic field, $(b^r, b^{\theta}, b^{\phi})$, as a function of radius and latitude. Proceeding in the same way as in Obergaulinger & Aloy (2017, 2020), we assume a large-scale geometry of the field restricted to the layers of the star which are magnetized. The radial and lateral components, on the one hand, and the azimuthal components, on the other hand, are respectively computed from the poloidal and the toroidal components of the stellar evolution model, all of them modulated by a factor $\sin \theta$. We note that, since the Taylor-Spruit dynamo is designed for radiative layers of stars, the magnetic field vanishes in convective layers by construction.

We present the structure of the progenitors at the onset of collapse in Fig. 1 and Fig. 2. In the former figure, the *top panel* displays the density profiles of the stars, the *mid panel* with profiles of the specific entropy gives an overview of the location of shell interfaces in the cores, and the *bottom panel* shows the compactness parameter (O'Connor & Ott 2011),

$$\xi(m) = (m/M_{\odot}) (1000 \text{ km}/r(m)), \quad (1)$$

defined by the mass m enclosed in a radius $r(m)$. The latter figure compares the profiles of specific angular momentum in the equatorial planes of the progenitors to the specific angular momentum of the last stable orbits for gas at a Lagrangian coordinate m orbiting black holes that would form from the collapse of all the matter inside of it. For those comparison profiles, we assume non-rotating and maximally rotating BHs as well as BHs whose angular momentum is equal to that of all the layers up to the mass coordinate m . Shells whose actual specific angular momentum exceeds the ones of the last stable orbits can be expected to form discs around BHs rather than directly fall into them (the mass coordinate where this happens is marked with a blue asterisk). Furthermore, layers of the stars with non-vanishing magnetic fields are shaded in these panels.

4 RESULTS

4.1 Overview

We summarize the outcomes of our simulations in Tab. 1, listing the explosion mechanism and the kind of compact remnant in comparison to the predictions of AD18 for the evolution of the stars where applicable. Model 16TI fails to launch an explosion during the entire time simulated and will produce a BH within a few more seconds. All other models experience delayed shock revival initiated by a combination of neutrino heating, non-spherical fluid flows, and

model	AD18	M_4	μ_4	$\mu_4 M_4$	\mathcal{R}_4	$\xi_{2.5}$	t_f [s]	t_{exp} [s]	$M_{\text{sh,e}}$ [M_\odot]	expl.	E_{exp} [10^{51} erg]	\mathcal{F}	remn.	M_r [M_\odot]	M_{Ni} [M_\odot]
35OC	--	2.15	0.20	0.43	113	0.49	2.6	0.19	1.9	$\nu/\text{M-E}$	1.2	5.5	BH	2.9	0.048
16TI	--	1.73	0.14	0.25	2.9	0.26	6.1	--	--	--	--	1.1	BH	2.8	--
A05	SLSN	1.82	0.11	0.21	0.70	0.20	3.7	1.7	2.1	$\nu\text{-E}$	1.9	0.40	PNS	2.2	0.011
A08	SLSN	1.72	0.09	0.16	1.4	0.16	4.8	3.4	2.1	$\nu\text{-E}$	0.43	0.54	PNS	2.2	0.0034
A13	SLSN	2.30	0.19	0.44	2.5	0.55	2.9	0.39	2.2	M-E	0.76	0.09	BH	2.6	0.050
A17	PM	2.07	0.05	0.11	0.76	0.17	3.9	1.7	2.1	$\nu\text{-E}$	1.1	2.2	PNS	2.1	0.0088
A20	PM	2.34	0.08	0.18	2.2	0.32	4.0	1.2	2.4	$\nu\text{-E}$	0.49	2.7	BH	2.5	0.011
A26	Co	2.76	0.21	0.58	2.9	0.71	1.5	0.56	2.5	M-E	0.98	1.5	BH	3.0	0.022
A30	Co	2.28	0.33	0.75	2.1	0.73	1.5	0.39	2.3	M-E	1.4	2.8	BH	3.0	0.036
A39	Co	1.97	0.12	0.25	2.6	0.37	3.8	0.51	2.1	$\nu/\text{M-E}$	0.56	5.8	BH	2.4	0.030

Table 1. Overview of models: model name, evolution according to AD18 (superluminous SN, PM with the potential to produce a GRB, or collapsar), properties of the stellar progenitor, M_4 (Eq. (2)), μ_4 (Eq. (3)), \mathcal{R}_4 (the rotational energy of the matter inside M_4 in units of [10^{48} erg]), and $\xi_{2.5} := \xi(2.5M_\odot)$ (Eq. (1)), our result: final and explosion times in seconds after bounce, the mass inside the shock wave at the onset of explosion ($M_{\text{sh,e}}$), the kind of explosion, the final explosion energy, E_{exp} and the free energy of the rotation of the PNS at the end of the simulation, \mathcal{F} , the type of remnant (the acronym BH is set in boldface if BH formation occurs during the simulation; in this case, the final simulation time is the BH formation time) and its mass at the final time, M_r , and an estimate for the expelled mass of Ni, M_{Ni} .

magnetorotational stresses. The importance of these effects as well as the time of explosion vary greatly across the mass range. In some cases, the explosion is sufficiently strong to quench accretion onto the PNS and prevent BH formation, but most cores, in particular at higher stellar masses ($M_{\text{ZAMS}} \geq 20M_\odot$), are likely to end up as BHs.

In the following, we will describe the most important features characterizing the evolution of several groups of models:

- (i) neutrino-driven explosions leading to NS or BH formation: models A05, A08, A17, A20, A39;
- (ii) MHD explosions with BH formation: models A13, A26, A30, 35OC;
- (iii) the failed explosion of model 16TI.

4.2 Neutrino-driven explosions

We will focus our discussion on models, in which arguments such as the ratio between the timescales of neutrino heating and of advection through the gain layer suggest that explosions are driven by neutrino heating aided by non-spherical flows. Models A05, A08, A17, and A20 undergo shock revival with a delay between $t_{\text{exp}} \approx 1.0$ s (A20) and $t_{\text{exp}} \approx 3.2$ s (A08) (see evolution of the maximum shock radius in *top panel* of Fig. 3). Model A39 explodes much earlier ($t_{\text{exp}} \approx 0.5$ s) and, showing a more pronounced influence of the magnetic field, could be considered an intermediate case between this class and that of MHD explosions (Sec. 4.3).

After the onset of the explosion, the shock wave expands at high speeds and the diagnostic explosion energies and ejecta masses (Fig. 3 *mid and bottom panels*) rise. By the end of the simulations, the explosion energies are around $E_{\text{ej}} \approx 5 \times 10^{50}$ erg s $^{-1}$ carried by $M_{\text{ej}} \approx 0.1 \dots 0.4 M_\odot$ of unbound gas. Both quantities keep increasing throughout the final phases of the simulation. Model A17 is an exception in that it shows a very rapid rise of E_{ej} by almost 10^{51} erg within about 0.5 s (starting at $t_{\text{pb}} \approx 3.1$ s) without a similar growth of M_{ej} . This quick rise, which does not show any sign of levelling off, corresponds to the activation of a wind powered by the magnetic spindown of the PNS, which by then has

turned into a proto-magnetar due to a growth of the surface field strength. This late-time evolution does not interfere with the revival of the SN shock wave.

The models of this group tend to possess the least compact cores among the progenitors considered here. As shown in Fig. 1, where this group is displayed using dashed lines, their density profiles, $\rho(m)$ (*top panel*), exhibit a strong decrease at mass coordinates $m < 2M_\odot$ near the location of the surface of the inner core, which in the *middle panel* show up as discontinuities in the specific entropy and the electron fraction. The comparably low densities further out correspond to moderate values of the compactness parameter, $\xi_{2.5}$, computed at $m = 2.5M_\odot$ according to Eq. (1), are listed in Tab. 1 (see also Fig. 1, *bottom panel*). These values are significantly below the threshold $\xi_{2.5} \approx 0.45$ of explodability stated in (O'Connor & Ott 2011) and, hence, these stellar models should easily yield successful supernova explosions. As a consequence of the low densities beyond the densest central part of the star, the models are characterized by low rates at which mass is accreted through the stalled shock wave in the pre-explosion phase (Fig. 3, *bottom panel*). Ertl et al. (2016) defined a two-parameter criterion for classifying the explodability of massive stars by the neutrino-driven mechanism. These two parameters are M_4 , defining the normalized enclosed mass for a dimensionless entropy per nucleon of $s = 4$,

$$M_4 \equiv m(s=4)/M_\odot \quad (2)$$

and μ_4 , the normalized mass derivative at this location

$$\mu_4 \equiv |(dm/M_\odot)/(dr/1000 \text{ km})|_{s=4} \quad (3)$$

The subset of models which produce neutrino-driven explosions, possess the smallest values of M_4 and of μ_4 of all the sample (Tab. 1). Precisely, small values of μ_4 are correlated with the small accretion rates observed for these models (Ertl et al. 2016). Likewise, the small values of the product $\mu_4 M_4$, correlate with the mass accretion rate onto the PNS (or through the shock). We consistently see in Tab. 1 that, indeed, the values of $\mu_4 M_4$ of models producing neutrino driven explosions are the smallest among all the models.

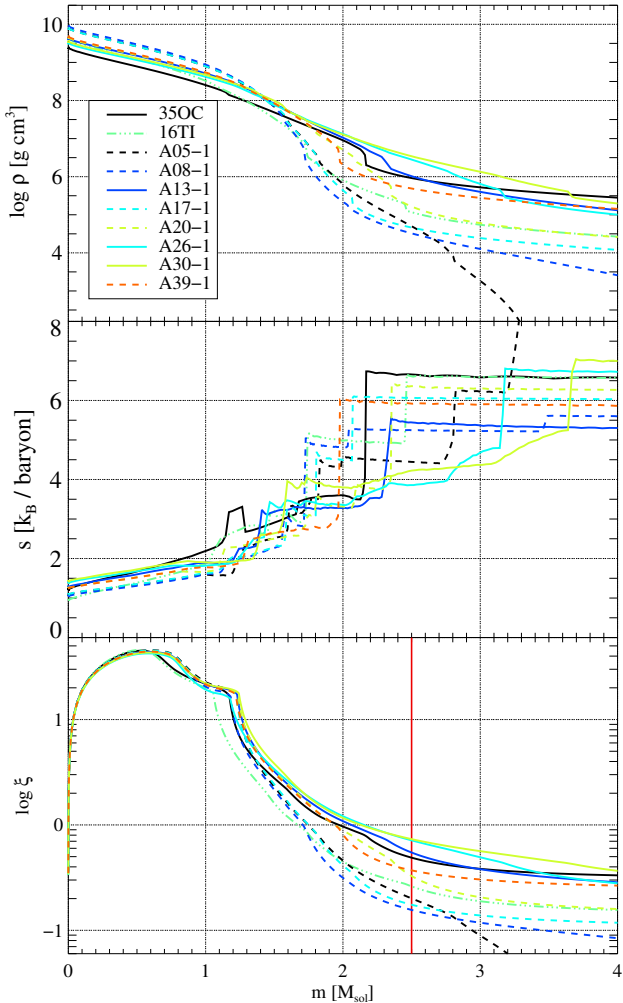


Figure 1. Top to bottom: profiles of density, specific entropy, and compactness of all progenitors at the onset of collapse. Models producing neutrino driven explosions, MHD effects or fail to explode are displayed with dashed, solid and dash-dotted lines, respectively.

Figure 6 represents the models of Tab. 1 in the $\mu_4 M_4 - \mu_4$ plane. The dashed line represents an approximate division of the plane in BH forming and PNS forming models according to Ertl et al. (2016). We observe that most BH forming models lie above the division line, but this is also the case for PNS forming models. Using other coefficients different from $k_1 = 0.283$ and $k_2 = 0.043$ the two-parameter classification criterion does not improve much (we have used all the possible combinations of k_1 and k_2 from Table 2 of Ertl et al. 2016). For the set of models at hand a better classification between BH forming and NS forming models is obtained for $k_1 \sim 0$, $k_2 \sim 0.12$. Also, a classification according to the rotational energy enclosed in M_4 is plausible. Stellar models with a rotational energy smaller than $\sim 1.4 \times 10^{48}$ erg yield PNSs, while above that limit the compact remnant is a BH (Tab. 1).

Despite the favourable conditions for explosions, it takes more than one second to achieve shock revival. Relative to the models exploding earlier due to MHD effects, these cores

tend to emit neutrinos at lower total luminosities (see Fig. 4, *upper panel*). The luminosities are not only lower in absolute values, but also relative to the gravitational energy of the PNSs. While, the production of neutrinos seems less efficient in this group of models, their effect on the dynamics is higher. This effect can be quantified by the ratio of the total neutrino luminosity to the mass accretion rate through the shock, $\zeta = L_\nu / (\dot{M} c^2)$ (*bottom panel*). Throughout the entire runs, models A05, A08, A17, A20, and models A39 show higher values of ζ than models exploding magnetorotationally. Their shock revival sets in when at $\zeta \gtrsim 1$. At that time, the mass in the gain layer has decreased to a few $10^{-3} M_\odot$ (Fig. 5, *top panel*). While the heating efficiency, $\eta_{\text{gain}} = Q_{\nu, \text{gain}} / M_{\text{gain}}$, rises until the explosion sets in (Fig. 5, *second panel*), the timescale at which the gas in the gain layer is heated by neutrinos, τ_{heat} , is, except for an episode around $t_{\text{pb}} \approx 0.1 \dots 0.2$ s, considerably longer than its advection timescale, τ_{adv} . The average of the ratio $\tau_{\text{adv}} / \tau_{\text{heat}}$ over the gain layer, shown in the *third panel*, rapidly rises above unity only immediately before the shock wave is revived. We note that, compared to model 35OC, all new models come closer to fulfilling the explosion criterion of $\tau_{\text{adv}} / \tau_{\text{heat}} = 1$ during an earlier phase of their evolution ($t_{\text{pb}} = 0.1 \dots 0.2$ s). The heating rate, however, does not suffice to increase the total energy of the gain layer to positive values. The failure can in part be attributed to a relatively low activity of non-spherical flows during this time. Furthermore, the magnetic energies in the gain layer are low and correspond to ratios between the advection time and the Alfvén travel time across the gain layer, $\tau_{\text{adv}} / \tau_{\text{Alf}}$, that are on average much less than unity (*bottom panel*). Hence, even taking into account a latitudinal variation of $\tau_{\text{adv}} / \tau_{\text{Alf}}$, the magnetic field contributes very little to reviving the shock wave.

After this phase, the models settle into a state maintained for a time between several hundreds of milliseconds and about 3 s characterized by a reduction of the mass accretion rate and a moderate contraction of the shock wave. Fairly constant neutrino luminosities translate into a timescale ratio $\tau_{\text{adv}} / \tau_{\text{heat}} \sim 0.3 \dots 0.6$. In models A08, A17, and A20, shock runaway is triggered by the quick decrease of the ram pressure corresponding to the infall of a shell interface located at a mass coordinate $m = 2.1 \dots 2.4 M_\odot$, while A05 reaches the transition to explosion without such an additional impulse due to a slow reduction of τ_{heat} over the course of about half a second. In the case of model A39, a non-negligible magnetic energy in the gain layer adds to the effect of neutrino heating and allows for an explosion at a much earlier time than in the other models ($t_{\text{exp}} \sim 0.4$ s).

The constraint of axisymmetry causes the ejecta to expand along the poles (Fig. 7). Variations in the fluxes of mass and energy lead to asymmetries of the outflows ranging from a moderate north-south imbalance to a unipolar geometry. Typically, the outflows coexist with cold downflows at lower latitudes that feed the growth of the PNS throughout the entire evolution after shock revival. As shown in the *bottom panel* of Fig. 7 displaying the central 600 km of the five models shortly before the end of the simulations, these downflows can take the form of narrow streams at high latitudes (A20), at lower latitudes (A39), as well as one-sided downflows across an entire hemisphere (A08). Transitions between these states can be observed. Consequently, the PNS mass (Fig. 8, *top panel*) exceeds $M_{\text{PNS}} = 2 M_\odot$ before the end of

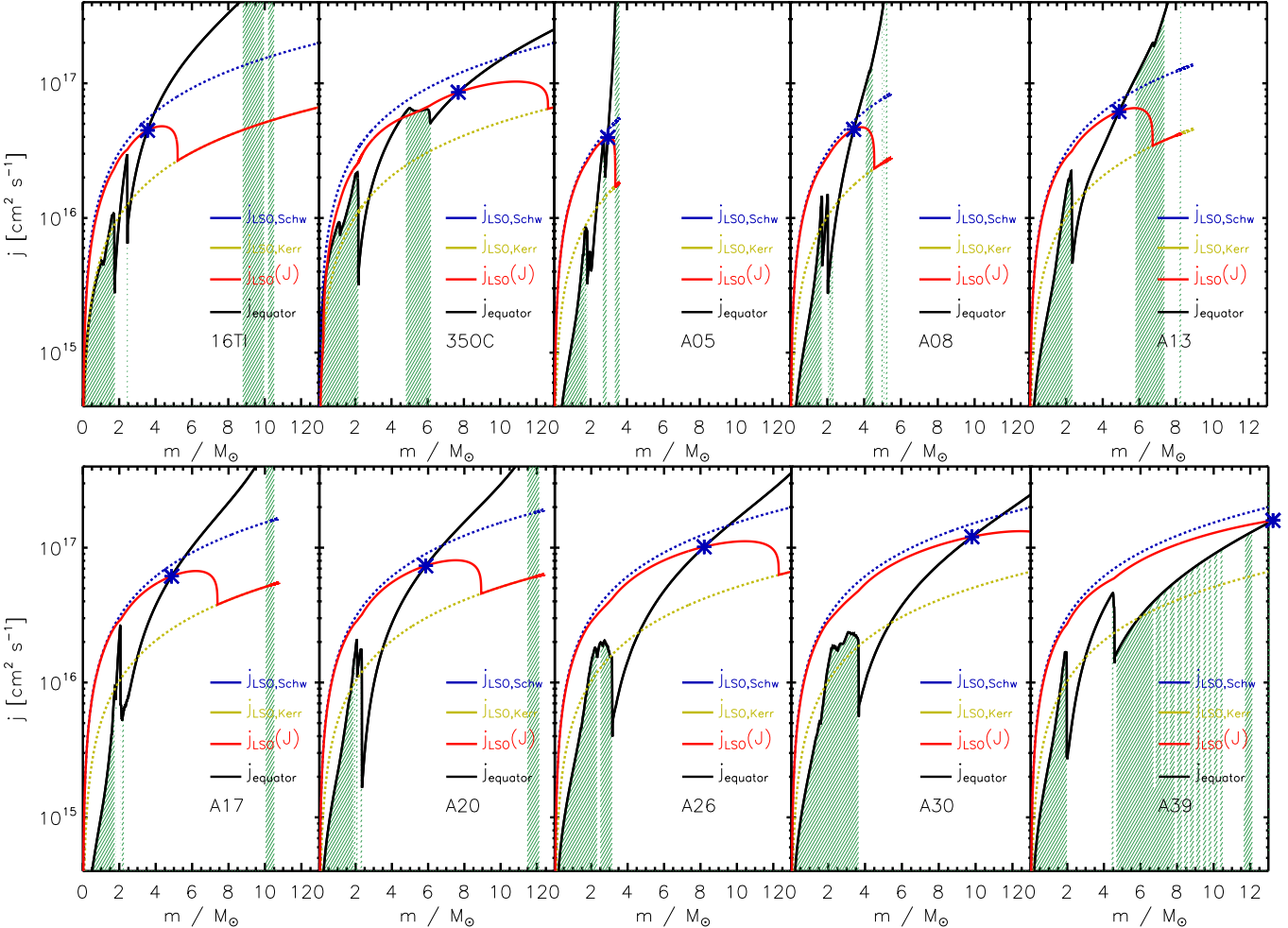


Figure 2. Equatorial profile of the initial specific angular momentum (black lines) of models as indicated in the panels. In each panel, the blue dashed lines denote the angular momentum needed to support matter at the LSO for a Schwarzschild BH, while the yellow dashed lines are for a Kerr BH with dimensionless spin $a = 1$. The red lines indicate the specific angular momentum at the LSO for a BH with the mass and angular momentum inside the displayed mass coordinate in the pre-SN star. The green-hatched parts of the plot denote the mass shells of the pre-SN star with non-zero magnetic field.

the simulations in all cases. For models A20 and A39, the final values of $M_{\text{PNS}} \approx 2.55 M_{\odot}$ and $M_{\text{PNS}} \approx 2.42 M_{\odot}$ correspond to BH formation. While model A08 was terminated with a considerably lower PNS mass of $M_{\text{PNS}} \approx 2.2 M_{\odot}$, the rate of accretion is similar to that of the aforementioned models and, thus, the collapse to a BH is a plausible outcome, too. Note, however, that the long-term evolution of the PNS is not necessarily monotonic in terms of, e.g. its mass growth, especially if sufficiently strong poloidal magnetic fields develop (Aloy & Obergaulinger 2021), as it is the case of model A08.

Models A05 and A17 show a transition to a phase in which accretion ceases to occur after $t_{\text{pb}} > 3$ s. No downflows reach the PNS. While matter is ejected at all latitudes, the velocities and mass fluxes are highest inside wide cones around the rotational axis (Fig. 7 *bottom panel*). At radii of a few 1000 km, these outflows are directed into wide polar jets (Fig. 7, *upper panel*). This configuration causes the PNSs to lose mass at rates of the order of $\dot{M}_{\text{PNS}} \sim -10^{-2} M_{\odot} \text{ s}^{-1}$ and signal a transient episode of PM spindown (transient episodes of PM spindown were also observed in models with

sufficiently strong poloidal field in Aloy & Obergaulinger 2021). The additional energy the spindown could add to the explosion is of the order of the free energy of the differential rotation of the PNS given by subtracting the rotational energy of a rigidly rotating body with the same angular momentum, J_{PNS} and inertial momentum, I_{PNS} , from the total rotational energy, $\mathcal{F} = \mathcal{T}_{\text{PNS}} - \frac{J_{\text{PNS}}^2}{2I_{\text{PNS}}}$ (see Tab. 1). In the case of model A17, this value is greater than the explosion energy at the end of the simulation, $\mathcal{F} \approx 2.2 \times 10^{51}$ erg, while for A05 it accounts only to a minor correction to the explosion.

All PNSs possess a high, albeit not excessively large, rotational energy. Final values of the rotational energy correspond to $\mathcal{T} = -E_{\text{PNS}}^{\text{rot}}/E_{\text{PNS}}^{\text{grav}} \sim 0.5\ldots 2 \times 10^{-2}$ (Fig. 8, *second panel*), i.e., a range in which the PNS might be susceptible to non-axisymmetric instabilities. Besides amplification processes inside the PNS, the evolution of the magnetic energy is mostly driven by the magnetization of the accreted matter. The final magnetic energies are typically two orders of magnitude lower than the rotational energies (Fig. 8, *bottom left panel*). Typical surface rotation rates reach a few 1000 s^{-1} (*upper right panel*) with models exploding mostly

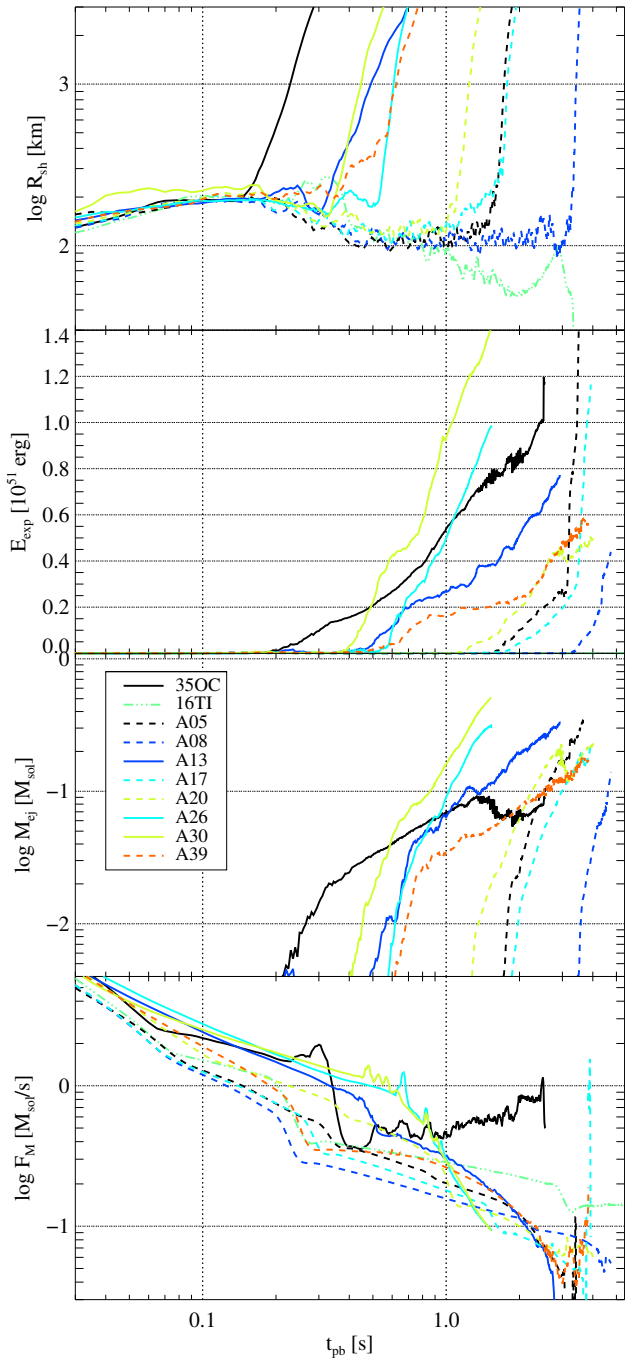


Figure 3. Top to bottom: shock radius, explosion energy, ejecta mass, and mass flux through the shock wave as functions of time.

due to neutrino heating found at the lower end of the distribution of Ω_{srf} . The average magnetic fields on the PNS surfaces are dominated by a toroidal component of the order of $B_{\text{srf}}^{\text{tor}} \sim 10^{14\text{--}15}$ G (Fig. 8, *mid right panel*). The poloidal components (*bottom right panel*) tend to be considerably weaker during most phases of the evolution, in some cases down to a mere $B_{\text{srf}}^{\text{pol}} \sim 10^9$ G. As stated above, the suppression of the poloidal field proceeds in concert with the burial of the surface field by non-magnetized accreted layers,

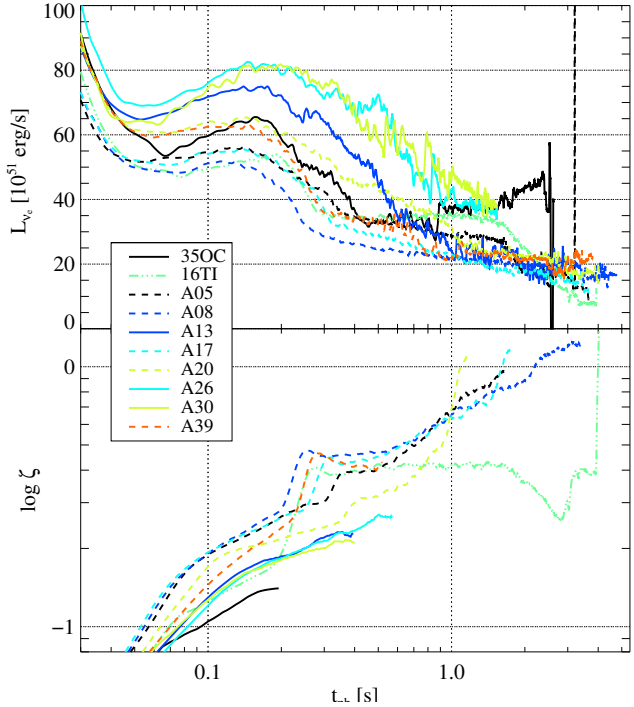


Figure 4. Top panel: luminosities of electron neutrinos. Bottom panel: ratio of the total neutrino luminosity to the mass accretion rate through the shock, ζ .

while the accretion of magnetized layers can lead to a quick rise of the poloidal field strength, exceeding $B_{\text{srf}}^{\text{pol}} \sim 10^{14}$ G and reaching equipartition with the toroidal component. Hence, the surface poloidal magnetic field of the models with smaller mass among the group that yields neutrino-driven explosions (A05, A08, and A17) grows to magnetar field strength after, at least $t_{\text{pb}} \sim 2.9$ s. Such conditions can favour the spin-down of the PNS and the transfer of its rotational energy to the surrounding gas, which then is accelerated and forms the aforementioned wind-like outflows of models A05 and A17.

4.3 Magnetorotational explosions

Models whose explosions are, as explained below, launched mainly by magnetic fields and rotation (350C, A13, A30, and, to a slightly lower degree, A26) exhibit shock revival after at most $t_{\text{exp}} \lesssim 0.5$ s (Fig. 3) and a steady increase of the explosion energies and masses, which for the two models based on progenitors with higher masses, A26 and A30, proceeds faster than for the lower-mass model A13 as well as for model 350C. The progenitors of A13 end with $E_{\text{exp}} \gtrsim 0.8 \times 10^{51}$ erg and $M_{\text{ej}} \gtrsim 0.3 M_{\odot}$.

The progenitors of this group possess more compact cores than those producing neutrino-driven explosions with higher densities and compactness parameters outside a mass coordinate of $m \approx 1.8 M_{\odot}$ (Fig. 1 *bottom panel*). Models driving magnetorotational explosions also have larger values of M_4 and of μ_4 as their neutrino-driven counterparts. These differences, related to their Fe cores containing more mass, translates into higher mass accretion rates through the shock (*bottom panel* of Fig. 3) and lower neutrino luminosities w.r.t. the mass accretion rate with ζ consistently

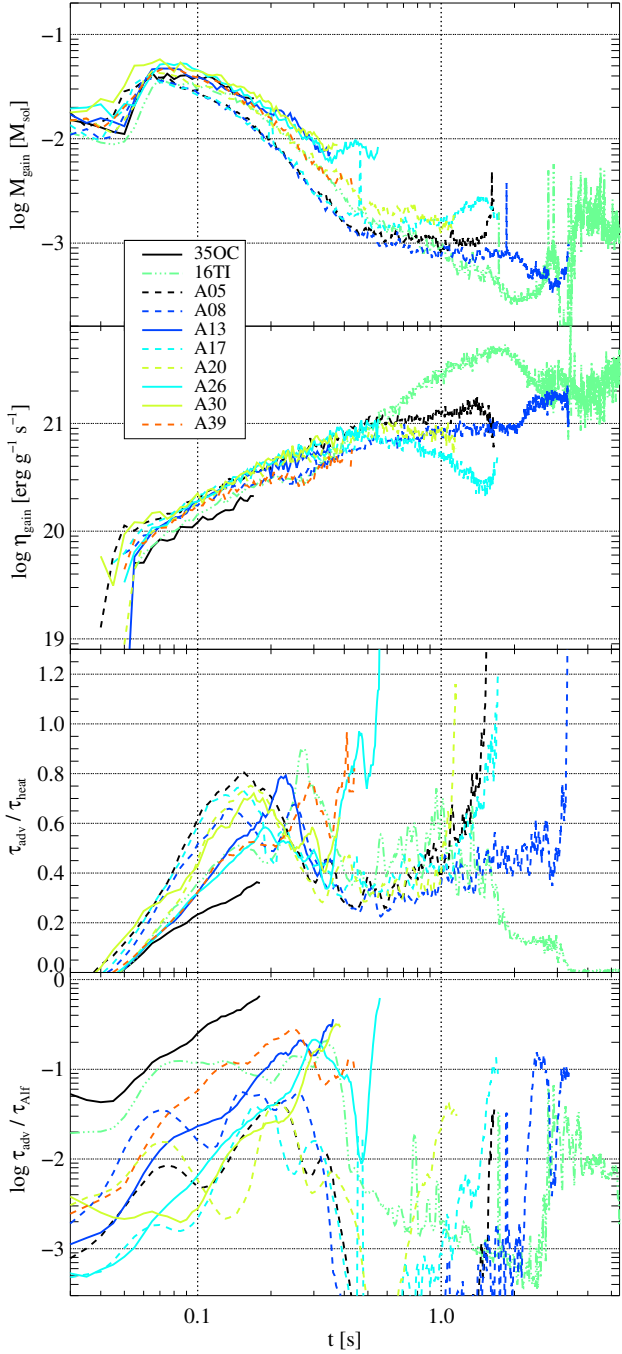


Figure 5. Top to bottom: mass in the gain layer, heating efficiency, ratio between advection and heating timescales, and between the advection and the Alfvén timescales. The lines and their colors are as in Fig. 4.

remaining below those of neutrino-driven explosions. These conditions make neutrino-driven shock revival more difficult to achieve.

The mass contained in the gain layers of these four models is on the upper end of the distribution (*top panel* of Fig. 5), while the rotational energies of the gain layer are lower than in the case of neutrino-driven explosions. The non-radial kinetic energies, on the other hand, do not

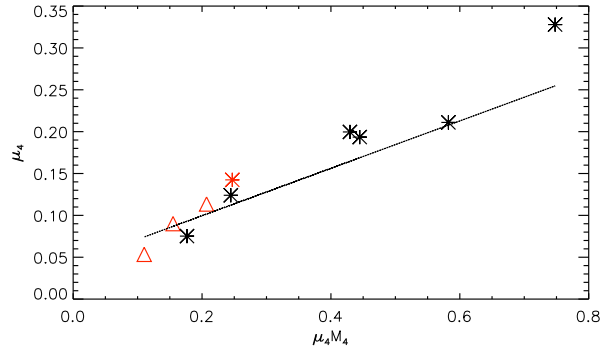


Figure 6. Representation of the computed models in the $\mu_4 M_4 - \mu_4$ plane. The dashed line corresponds to $y = 0.283x + 0.043$, where $y = \mu_4$ and $x = \mu_4 M_4$. Black asterisks identify models of Tab. 1 that yield BHs, while red triangles correspond to models that do not form BHs. The red asterisk represents model 16TI, which has not formed a BH by the end of the computed time.

systematically deviate from the other models, suggesting a similar level of hydrodynamic instabilities and turbulence. At least within the group of models from AD18, the same holds for the heating efficiency, η_{gain} (Fig. 5 *mid panel*). As a consequence, the models show a similar evolution of the advection-to-heating timescale ratio, $\tau_{\text{adv}}/\tau_{\text{heat}}$ with an early rise that by $t_{\text{pb}} \lesssim 200$ ms stops around $\tau_{\text{adv}}/\tau_{\text{heat}} \approx 0.8$, i.e., at values that can be regarded insufficient for launching an explosion (*bottom panel*).

Model 350C possesses a relatively high magnetic energy in the gain layer already shortly after bounce. The three models from AD18 start with a much weaker magnetization in the gain layer, but the accretion of extended layers with non-zero magnetic field (cf. Fig. 2) causes the magnetic energy to rise to values around $E_{\text{gain}}^{\text{mag}} \gtrsim 10^{47}$ erg. Models A13 and A30 explode shortly after that point. In these cases, the average ratio between the advection and the Alfvén timescale, $\tau_{\text{adv}}/\tau_{\text{Alf}}$, is still significantly lower than unity (Fig. 5, *bottom panel*). However, since the magnetic field is much stronger along the rotational axis than at lower latitudes, the Alfvén timescale becomes comparable to the advection timescale locally, giving rise to polar shock revival (as discussed in Obergaulinger & Aloy 2020). The shock wave of A26 ceases to propagate after a short outward displacement and is revived only after a delay of another about 150 ms, when the timescales for neutrino heating and for Alfvén waves locally reach values similar to that of advection.

To a larger degree than for neutrino-driven shock revival, the different ejecta, whose entropy distributions are displayed in Fig. 9 at the time when the maximum shock radius reaches 1000 km, are propagating in narrow jets along the rotational axis. The flow speeds in the jets reach up to $v^r \gtrsim c/3$ at radii of a few 1000 km with models A26 and A30 producing faster ejecta, followed by model A13. Downflows near the equatorial plane, found in all models, are persistent and lead to a comparably rapid growth of the PNS mass. Models A26 and A30 surpass the limit for stability of non-rotating neutron stars within less than ≈ 0.6 s. The growth proceeds until $M_{\text{PNS}}^{\text{A26, A30}} \approx 3 M_{\odot}$, at which point not even the rotational energy corresponding to

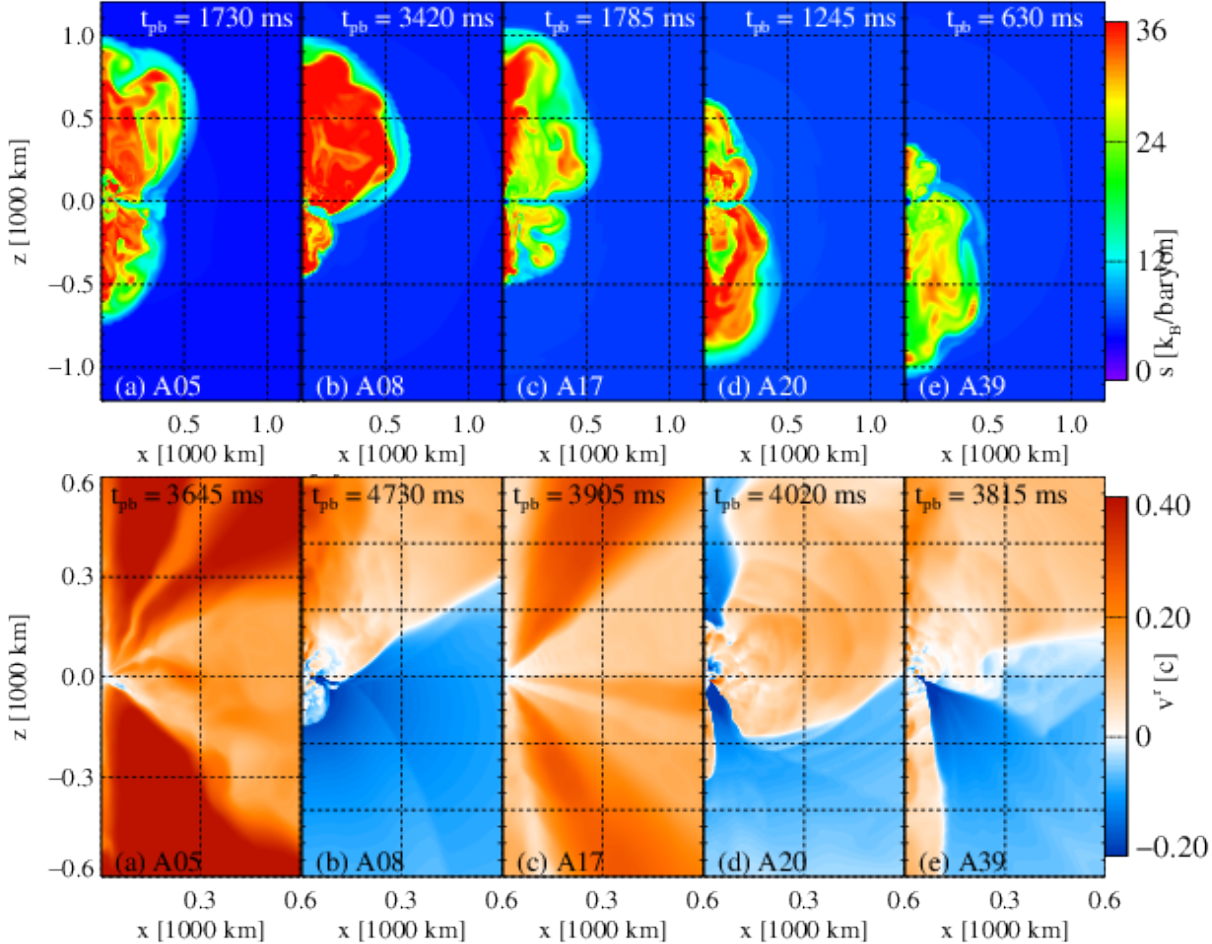


Figure 7. Top: Entropy maps of neutrino-driven explosions at the time when the shock wave has reached a maximum radius of $r_{\text{sh}} \approx 1000$ km. Bottom: maps of radial velocity towards the end of the runs.

$E_{\text{PNS}}^{\text{rot}, \text{A26, A30}} \approx 0.03 E_{\text{PNS}, \text{A26, A30}}^{\text{grav}}$ and a high degree of differential rotation can prevent the PNS from collapsing to a BH. Reaching gravitational instability takes longer for the less compact model A13. The magnetic influence on the explosion is not reflected in a particularly high magnetic energy of the PNSs. Compared to model 350C, the ratio of magnetic to rotational energy is lower by at least an order of magnitude. Indeed, the evolution of the ratio $E_{\text{PNS}}^{\text{mag}}/E_{\text{PNS}}^{\text{rot}}$ is very different in CHE models compared to the models of Woosley & Heger (2006). The former models possess much larger initial core rotational energies, which translate into ratios $E_{\text{PNS}}^{\text{mag}}/E_{\text{PNS}}^{\text{rot}}$ orders of magnitude smaller than in non-CHE models. The large differential energy reservoir of CHE models is partly tapped into by magnetic energy, making $E_{\text{PNS}}^{\text{mag}}/E_{\text{PNS}}^{\text{rot}}$ comparable to or larger than for non-CHE models after $t_{\text{pm}} \gtrsim 2$ s (Fig. 8 bottom left). The magnetic field strengths on the PNS surfaces, on the other hand, are much stronger than for the neutrino-driven explosions. The poloidal component in particular is consistently around $B_{\text{srf}}^{\text{pol}} \sim 10^{13}$ G.

Based on these results, we suggest that the presence of (moderately) strong, large-scale magnetic fields connecting the PNS surface to and beyond the gain layer is the main reason for the ability of models 350C, A13, A26, A30 to launch explosions despite their high compactness and despite not featuring particularly high neutrino heating rates.

It is precisely this subset of progenitors which possesses a magnetized layer around a mass coordinate of $m \approx 2 M_{\odot}$ (shaded regions in Fig. 2), whereas the absence of such a layers seems to preclude the possibility of MHD explosions. We note that the intermediate case of model A39 exhibits a magnetic field up to almost this mass coordinate and that the model A17 accretes a rather narrow shell with non-vanishing magnetic field around the time when it accelerates a late outflow resembling proto-magnetar winds. Model A05 produces a similar outflow after the (poloidal) PNS surface field has grown by several orders of magnitude without accreting a magnetized layer. This suggests a second way to create the field configuration necessary to launch such an outflow by transporting field from the interior of the PNS to its surface or amplifying it locally.

4.4 Failed explosion

The evolution of model 16TI is affected strongly by its very rapid rotation. In the innermost $m \approx 2 M_{\odot}$, its initial density profile, the compactness derived from it, the parameters M_4 and μ_4 roughly fall into the range established by models exploding due to neutrino heating. Consequently, the mass accretion rate is, at least at early times, comparable to those. At the same time, centrifugal support reduces

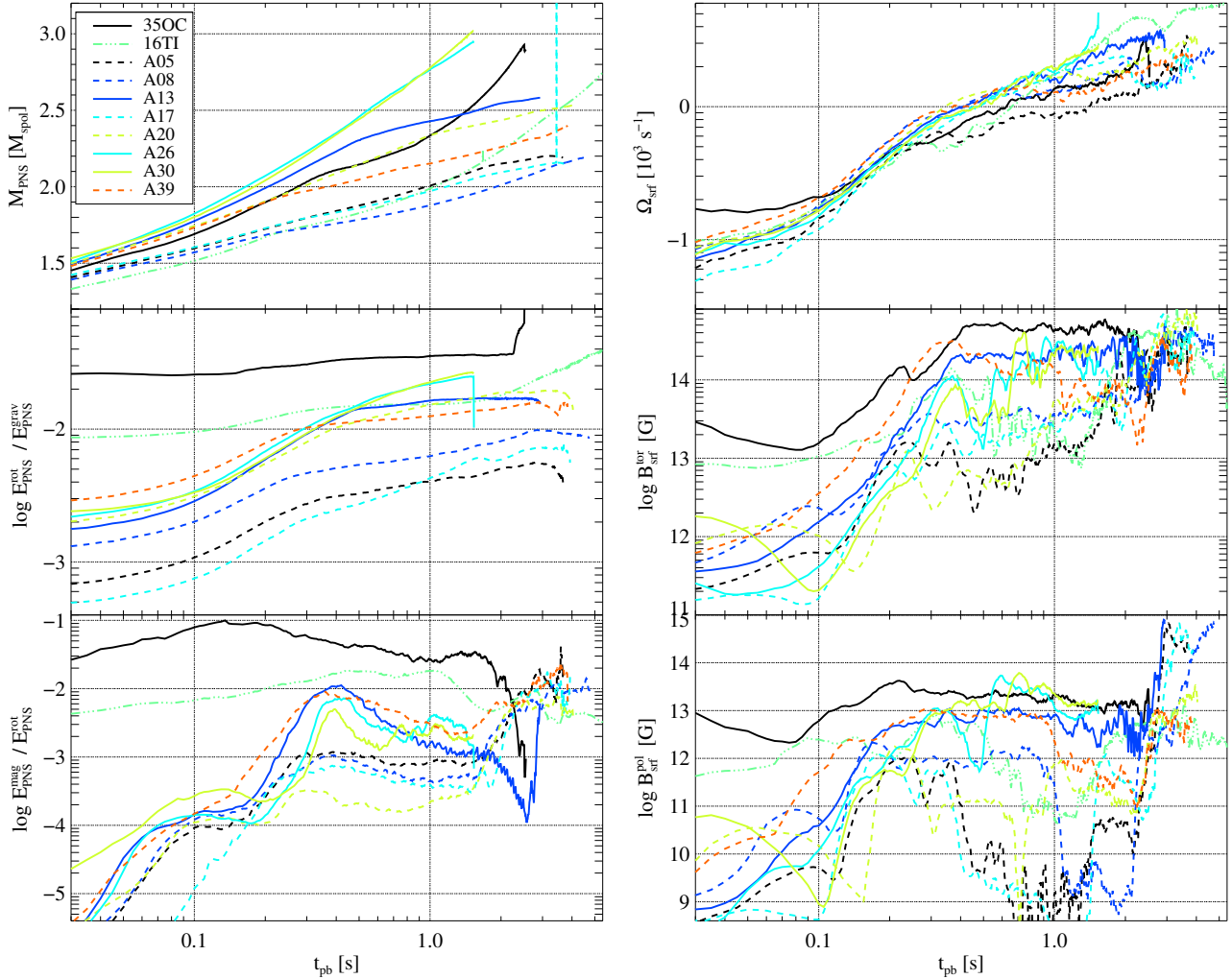


Figure 8. Left panel, top to bottom: evolution of the mass of the PNSs, the rotational energy normalized by the gravitational energy, and the magnetic energy normalized by the rotational energy. Right panel, top to bottom: averages of the rotational velocity, the toroidal and poloidal magnetic field strengths over the PNS surfaces.

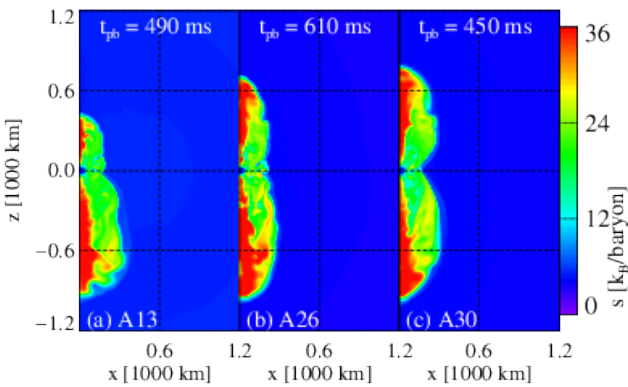


Figure 9. Same as the *top panels* of Fig. 7, but for magnetorotational explosions.

the release of gravitational energy from the matter falling onto the PNS, thus lowering the neutrino luminosity. After $t_{\text{pb}} \approx 0.25$ s, when the entire inner core has been accreted,

this reduction becomes less important, but then a relatively shallow density profile causes the mass accretion rate to drop only slowly. Measured in terms of the mass accretion rate, the neutrino luminosity never gets high enough to trigger an explosion with $\zeta \sim 0.4$ for most of the evolution. Until $t_{\text{pb}} \sim 2$ s, neutrino heating is still fairly important in a gain layer whose mass is shrinking below $M_{\text{gain}} < 10^{-3} M_{\odot}$. Advection through the gain layer remains faster than neutrino heating, though only by a factor of about 2.

We note that model A39 launches an explosion under conditions that are not too dissimilar from the state of failing model 16TI. The former model, however, possesses a magnetic field that is sufficiently strong to aid in the process of reviving the shock wave. In model 16TI, on the other hand, once the entire Fe core has fallen onto the PNS, the ensuing drop of the mass accretion rate goes along with a transition to the accretion of a non-magnetized shell. Hence, the magnetization of the gain layer drops, eliminating the prospects of an explosion due to a mixed neutrino-MHD mechanism like in model A39.

Failing to launch an explosion, the model is bound to produce a BH as M_{PNS} steadily increases. By $t_{\text{pb}} \gtrsim 3$ s, the PNS exceeds the limit for stability for a non-rotating NS. However, its very high rotational energy delays the collapse by several seconds and allows for the accretion of additional mass.

In the time interval $t_{\text{pb}} \approx 2.6\text{...}3.2 s, the layers located in the progenitor at Lagrangian mass coordinates $m \approx 2.32\text{...}2.45 M_{\odot}$ are falling onto the PNS. These layers possess a particularly high specific angular momentum in excess of our estimates for the angular momentum corresponding to the last stable orbit for a maximally rotating Kerr BH encompassing all the matter enclosed by them (Fig. 2; note the yellow dashed line). Their fall onto the PNS is visible in the *bottom* panel of Fig. 10 showing the evolution of the specific angular momentum of gas in the equatorial plane as a function of time and radius. To further illustrate the effect of rotation on the structure of the core, we compare the profiles of $j(m)$ in the equatorial plane for several times (solid lines in the *top* panel of the figure) to the specific angular momentum of matter in Keplerian rotation about the centre, defined as $j_{\text{Kep}} = r^2 \sqrt{-\Phi}$, where Φ is the gravitational potential (dashed lines). The accretion can be stopped by the centrifugal forces where $j > j_{\text{Kep}}$, which is the case during this phase. Consequently, we observe the formation of a small rotationally supported torus just above the PNS surface. As displayed in Fig. 11 for $t_{\text{pb}} = 2.8$ and 3.1 s, this torus is located directly adjacent to the PNS and extends from its surface to about twice its radius. The torus is composed of matter with densities of $\rho > 10^{11} \text{ g cm}^{-3}$ (black contours). This high density makes it partially optically thick to neutrinos and the neutrinospheres (pink lines) encompass large swaths of it. In the central regions of the torus, the emission of neutrinos occurs on rapid timescales compared to the dynamics and dominates over their absorption. Consequently, the matter approaches an equilibrium state characterized by low entropy and low electron fraction, the absorption equilibrium of Just et al. (2021).$

Since the distribution of j shows an abrupt decline toward higher radii, gas accreted after $t_{\text{pb}} \approx 3.2$ s comes with much lower specific angular momentum. After only a brief time, the centrifugal support of the torus no longer suffices to balance gravity and the ram pressure of the newly accreted gas, and the torus breaks down and is quickly absorbed by the PNS. In the subsequent seconds of the evolution, the specific angular momentum of the accreted gas remains below the Keplerian value by a factor of a few. The structure of the core does not change from the state displayed in the *right* panel of Fig. 11. The PNS is separated from the infalling matter by only a very thin layer of hot gas with high electron fraction. This configuration may only change when the PNS collapses to a BH or when the next layer with potentially super-Keplerian rotation, located at a mas coordinate of $m \approx 3.1 M_{\odot}$ will be accreted. The PNS can only sustain itself against its own gravity until this point due to its fast rotation. Hence, any sufficiently efficient process leading to a loss of angular momentum to the exterior or a flattening of the differential rotation, such as non-axisymmetric instabilities or magnetic fields acting on secular timescales might lead to BH collapse before the accretion of this layer can produce another PNS-plus-torus system.

We note that we had observed the formation of a qualitatively similar system in previous models such as 350C-Rw, 350C-RRw or 350B-RRw (Aloy & Obergaulinger 2021), which also shows a very extended disc around the PNS. In that case, however, the disc formation was an inside-out process driven by the magnetic transport of angular momentum from the centre of the PNS to its outer layer, which consequently gain centrifugal support and expand. Here, on the other hand, the torus is formed due to the high angular momentum the gas possesses already in the pre-collapse state. Hence, contrary to the inside-out mechanism, for which the disc forms from gas belonging to the PNS, the outside-in process relies on neutrino emission to drive Y_e to the low values we find in model 16TI.

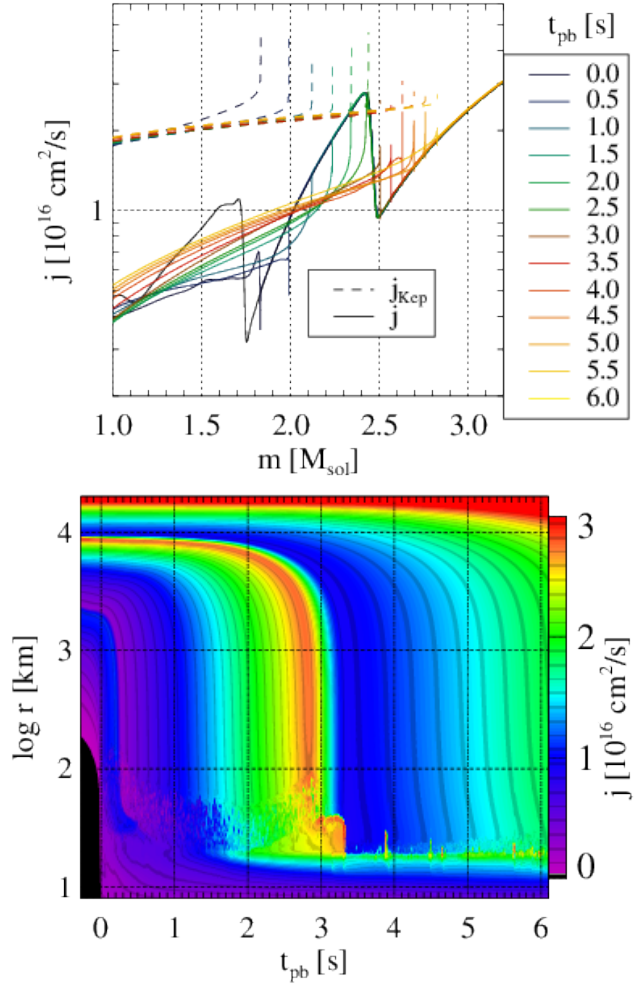


Figure 10. Top panel: profiles of the actual specific angular momentum in the equatorial plane of model 16TI (solid lines) compared to the Keplerian specific angular momentum (dashed lines). Bottom panel: specific angular momentum in the equatorial plane of model 16TI as a function of time and radius.

tatively similar system in previous models such as 350C-Rw, 350C-RRw or 350B-RRw (Aloy & Obergaulinger 2021), which also shows a very extended disc around the PNS. In that case, however, the disc formation was an inside-out process driven by the magnetic transport of angular momentum from the centre of the PNS to its outer layer, which consequently gain centrifugal support and expand. Here, on the other hand, the torus is formed due to the high angular momentum the gas possesses already in the pre-collapse state. Hence, contrary to the inside-out mechanism, for which the disc forms from gas belonging to the PNS, the outside-in process relies on neutrino emission to drive Y_e to the low values we find in model 16TI.

5 POTENTIAL FUTURE EVOLUTION

Except for gravitational waves and neutrinos, no sign of the dynamics would be visible for an external observer by the end of our simulations. Hence, any attempt to determine the type of explosion from the state at this point is beset

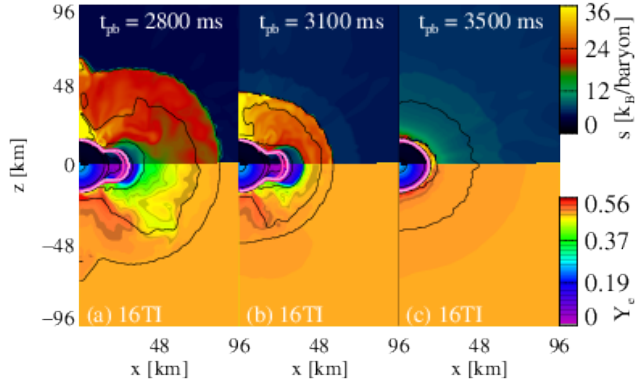


Figure 11. Specific entropy and electron fraction (colour maps) together with isodensity lines ($\rho = 10^{15, 14, 13, \dots} \text{ g cm}^{-3}$, black lines) and the neutrinospheres (pink lines) of model 16TI around the temporary formation of a rotationally supported disc around the PNS.

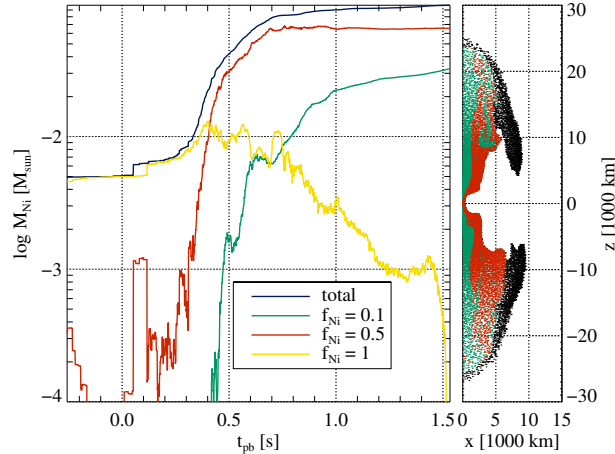


Figure 12. *Left panel:* time evolution of the ejected Ni mass of model A30. The dark blue line represents the total Ni mass, and the coloured lines show the mass contained in gas with a production factor f_{Ni} as indicated in the legend. *Right panel:* spatial distribution of unbound fluid elements at the end of the simulation. Black symbols stand for Lagrangian tracers that do not contain any Ni, while tracers with $f_{\text{Ni}} = 0.1, 0.5, 1$ are displayed by the same colours as in the *left panel*. The yellow Lagrangian tracers are very scarce at the end of the computed time and, hence, hardly visible at the interface between the jet cavity and the progenitor star.

with large uncertainties. In addition to the diagnostic explosion energies, ejecta geometries and the type of compact remnant, we consider a very rough estimate of the mass of radioactive Ni synthesized and ejected. In a manner similar to the flashing scheme our EOS uses to determine the composition of the baryonic component of the gas Rampp & Janka (2002); Müller et al. (2016), we assume that a fraction $f_{\text{Ni}} \leq 1$ of all lighter elements contained in an unbound fluid element of the ejecta is immediately burned to Ni once the temperature exceeds a threshold of $T_{\text{Ni}} = 5 \text{ GK}$. At sufficiently high entropy per baryon, photodisintegration of Ni into α particles may significantly limit the amount of Ni synthesized. Based on the work by Surman et al. (2011), Hayakawa & Maeda (2018) account for this effect by com-

puting the specific entropy of the baryons,

$$s_{\text{b}} = \frac{4a_{\text{rad}}m_pT^3}{3\rho k_{\text{B}}}, \quad (4)$$

where a_{rad} , m_p , and k_{B} are the radiation constant, the proton mass, and Boltzmann's constant, respectively. The Ni fraction depends on s_{b} ,

$$f_{\text{Ni}} = \begin{cases} 1 & \text{for } s_{\text{b}} < 1, \\ 0.5 & \text{for } 1 < s_{\text{b}} < 10, \\ 0.1 & \text{for } 10 < s_{\text{b}}. \end{cases} \quad (5)$$

We adopt the same approximation. In practice, we record the evolution of Lagrangian tracer particles. If the temperature of a tracer surpasses T_{Ni} , we assign it a fraction of Ni according to its entropy. This fraction can change as long as the temperature is higher than T_{Ni} . After cooling below this value, the composition is assumed to freeze out.

Note that our simulations use an EOS that contains, in addition to baryons, also leptons and photons. These additional components make the entropy in our simulations in general greater than the approximation of Hayakawa & Maeda (2018). To use their recipe together with our EOS, we would have to recalibrate the entropy thresholds to account for the systematic differences. Such an improvement of the method would require a detailed comparison to the conditions for NSE and is beyond the scope of this article. We cautionary note that our simple estimates can be off by several 10 %.¹ Thus, we only use them to obtain general tendencies within our set of stars. The results are listed in the last column of Tab. 1 as M_{Ni} .

We discuss the results of a representative case, model A30, for which the time evolution of the Ni mass and the spatial distribution of Ni at the final time are shown in Fig. 12. Some of the fluid elements that will be ejected already contain Ni before bounce, $t_{\text{pb}} < 0$. At that time, they possess low entropy and, thus, consist entirely of Ni ($f_{\text{Ni}} = 1$, yellow line in the *left panel*). In the first phase after bounce, most ejecta that surpass T_{Ni} do so at low entropy and therefore belong to the same group. However, as neutrino heating and shock waves in the jet increase the entropy of the tracers, some of the Ni is dissociated and f_{Ni} decreases for the aforementioned fluid elements, while additional Ni production occurs mostly in tracers with higher entropy and, thus, low $f_{\text{Ni}} = 0.5$ and 0.1 (red and green lines, respectively). At the end of the simulation, the Ni content of the model is dominated by gas with $f_{\text{Ni}} = 0.5$, mostly distributed in the cocoon of the jet (red points in the *right panel*), while the jet beam contains matter with higher entropy and $f_{\text{Ni}} = 0.1$ (green symbols). Ejecta that never reached the threshold temperature for Ni formation can be found surrounding the jets.

At first glance, the Ni masses synthesized in our models are insufficient to even explain typical CCSNe, which yield $\sim 0.1M_{\odot}$ of Ni. Even less can they account for more

¹ For comparison, using a detailed nucleosynthesis network, Reichert et al. (2021) obtained $M_{\text{Ni}} = 0.0473M_{\odot}$ for model 350C. For the same model, we obtain with the simplified method here described $M_{\text{Ni}} = 0.048M_{\odot}$. The striking similarity of the results should not be taken as a measure of the goodness of the simplified treatment. Applied to other models of Reichert et al. (2021), discrepancies of a few 10% are found.

energetic hypernovae, which produce larger amounts of Ni (Iwamoto et al. 1998; Drout et al. 2011; Lyman et al. 2016). However, we first note that all our models, save for the non-exploding model **16TI**, show (diagnostic) explosion energies of the order of the canonical value of $E_{\text{exp}} = 10^{51}$ erg or more (see Tab. 1). Extrapolating to subsequent phases, further growth is possible, unless the collapse of the PNS to a BH shuts down the injection of energy into the surrounding gas. But even if that happens, after the formation of a collapsar, further Ni can be synthesized in the winds emerging from the accretion disk (e.g. MacFadyen et al. 2001; Kohri et al. 2005; Kumar et al. 2008; Hayakawa & Maeda 2018), but exploring this regime is beyond the scope of this paper. Also, some extra Ni production can be expected from explosive nucleosynthesis due to the interaction of this wind with the stellar envelope (Woosley & Weaver 1995; Maeda & Tominaga 2009). However, this mechanism tends to operate once the BH is sufficiently massive, as it has swallowed most of the stellar envelope. That limits the availability of envelope materials for explosive nucleosynthesis (Maeda & Tominaga 2009), specially in CHE models with masses below, say, $8M_{\odot}$ (i.e., **A05**, and **A08**). These models may, at most, form BHs as massive as their initial pre-SN mass minus the ejecta mass. Neutrino-driven explosions are systematically less violent than magnetorotational ones. Models **A05** and **A17**, which, after a shock revival powered by neutrino heating, enter a proto-magnetar-like phase in which the explosion energy increases at very high rates. While all explosions show an asymmetric geometry, to a certain degree enforced by the assumption of axisymmetry, a stronger contribution of magnetic fields to the explosion enhances this tendency.

According to these findings, model **A17** seems the most likely candidate for launching a GRB within the proto-magnetar scenario accompanied by a moderately luminous SN. Model **A05** might evolve along similar lines, and model **A08**, which also may leave behind an NS rather than a BH, would be characterized by an SN at the upper end of the usual range of energies and luminosities that might be followed by a PM-driven GRB.

Among the BH-forming stars, model **16TI** represents the clearest case for a collapsar. While it, at least up to this point, fails to produce an SN, the other stars from this group tend towards high values of M_5 , possibly indicative of rather bright explosions as we expect those parts of the ejecta that have reached the highest radii to continue their propagation even after BH formation. Given their progenitor structure, which enables the possibility of forming an accretion disc, a collapsar phase could develop within a few seconds.

6 CONCLUSIONS

To explain some of the most extreme classes of stellar core collapse, viz. SLSNe and GRBs, rotation and strong magnetic fields have been invoked. However, for high-mass stars serving as progenitors of CCSNe to develop these elements requires special evolutionary scenarios. AD18 explored such a possibility in stellar-evolution models of stars with enhanced rotational mixing leading to CHE which ended their hydrostatic burning phases as Wolf-Rayet stars. Based on approximate methods, they found that several of their models with masses between $M_{\text{ZAMS}} = 5M_{\odot}$ and $M_{\text{ZAMS}} =$

$39M_{\odot}$ might explode as SLSNe or as GRBs powered by PMs or collapsars.

We used self-consistent two-dimensional numerical simulations of eight of their progenitors to check these estimates and constrain likely endpoints of the evolution. To this set, we added two rapidly rotating progenitors from Woosley & Heger (2006), model **350C** with $M_{\text{ZAMS}} = 35M_{\odot}$ from our previous studies and model **16TI** ($M_{\text{ZAMS}} = 35M_{\odot}$) that has been employed in various studies of the propagation of jets produced by GRB engines through stellar envelopes. The simulations included special relativistic MHD, an approximately general relativistic gravitational potential, spectral two-moment neutrino transport, and the relevant reactions between neutrinos and matter.

While we are able to run the simulations for very long times, even longer run times would be desired, e.g., to go beyond the formation of a BH, which is currently not feasible with the same approach to the detailed modelling of the microphysics. Furthermore, the assumption of axisymmetry might artificially restrict the dynamics of the stellar cores, in particular when it comes to possible spiral modes of the PNS and the post-shock region Ott et al. (2005); Blondin & Shaw (2007); Fernández (2010), the amplification of the magnetic field and dynamos Endeve et al. (2012); Mösta et al. (2015), and the stability of magnetically driven outflows Mösta et al. (2014); Obergaulinger & Aloy (2021). Multi-dimensional simulations may also hold the key to removing some of the biggest uncertainties regarding the progenitor, viz. the structure of the magnetic field, in particular in convective layers.

All of our models, save for model **16TI**, eventually produce explosions. We find shock revival due to neutrino heating and explosions driven by the magnetorotational mechanism. The latter class of explosion is possible if the PNS and the gain layer possess a strong magnetic field. Whether or not this condition can be fulfilled depends on the distribution of the magnetic field in the progenitor star (in agreement with the findings of Bugli et al. 2020; Aloy & Obergaulinger 2021). The stellar evolution calculations account for magnetic fields only in radiative layers and neglect them in convective zones. Hence, the gain layer may possess a strong field when a radiative zone is falling through the shock wave, while being only weakly magnetized during the accretion of a convective layer. This connection with the stellar profile makes MHD explosions viable for the stars from AD18 with ZAMS masses of $M_{\text{ZAMS}} = 13, 26$, and $30M_{\odot}$, besides our model **350C**. In the other models, shock revival is primarily or entirely driven by neutrino heating and non-spherical gas flows. The large masses of the stellar cores translate in very late explosions in some of the models, in particular at the lower end of the mass range. Once launched, the explosions assume a polar geometry with a more or less pronounced north-south asymmetry. The diagnostic explosion energies are moderate to high with maximum values of up to $E_{\text{exp}} \approx 1.9 \times 10^{51}$ erg, though it should be noted that it is still growing by the end of the simulations in most models. Furthermore, for models that form PNSs, the free rotational energy in the compact remnant may be tapped by the PM and contribute to the light curve of the SN explosion at later times. This energy can be as large as twice E_{exp} in some models (e.g., in **A17**).

Before and after the explosion, mass accretion increases

the masses of the PNS, in some cases driving it above the limit for gravitational stability. Rotation can allow for the PNS to reach a mass close to $M_{\text{PNS}} \approx 3 M_{\odot}$ before collapse. Our simulations end at BH formation or after a few seconds of post-bounce evolution. Hence, our prospects to confirm or disprove the predictions of AD18 regarding the fate of the stars are limited. However, the expected neutron star masses in models that do not form BHs exceed $2M_{\odot}$, categorising them as massive neutron stars according to Antoniadis et al. (2016).

Although the number of models that we have explored here is very small compared to the large sample of neutrino-driven explosions conducted in Ertl et al. (2016), we find that the two-parameter criterion for the remnant prediction only marginally applies for rotating, magnetized and low-metallicity stars. BH forming models typically form with $\mu_4 > 0.12$, but model **A20** challenges this rough division. Instead, a one parameter division according to $\xi_{2.5}$ appears as a simple criterion to distinguish between BH forming ($\xi_{2.5} \geq 0.21$) and PNS forming cases ($\xi_{2.5} < 0.2$). Likewise, a division based upon the rotational energy contained within M_4 allows for a rough classification of the potential remnants: low rotational energies in the pre-collapse stellar matter with $s \leq 4$ ($\leq 1.4 \times 10^{48}$ erg) produce PNSs as compact remnants. However, we note that these results apply to axisymmetric models. In 3D the accretion rate onto the PNS may be significantly lowered and the prospects to produce PNSs might be increased (Obergaulinger & Aloy 2021). More systematic studies, including finer grids of models and extended to 3D, will be the subject of future work.

The clearest indication for PM activity can be found in models **A17** and **A08** where a rapidly rotating and strongly magnetized PNS with too little mass for a BH to form accelerates an MHD wind and injects energy at a high rate into the ejecta. If the model maintained its structure for a substantial time, it would, as suggested by AD18, power a PM-driven GRB. The explosion energies of the two low-mass models, **A05** and **A08**, do not reach particularly high values by the end of the simulation. However, given the rates at which they increase and the strong surface fields of the PNS hint at the possibility of additional magnetorotational energy input on longer timescales. Whether this prospect manifests in the form of an SLSN or a GRB cannot be answered without much longer simulation times.

In all other cases, the PNS collapses to a BH within a few seconds. At their formation, the BHs rotate at only moderate rates with initial spin parameters between $a \approx 0.3$ and $a \gtrsim 0.5$. Mass accretion continues at rates of several $0.01 M_{\odot} \text{s}^{-1}$. Thus, within several hundreds of seconds, the shells at mass coordinates at $m \approx 3M_{\odot}$ will fall towards the centre. These shells possess a specific angular momentum around $j \gtrsim 10^{16} \text{ cm}^2 \text{s}^{-1}$, which would allow for the collapsar-driven GRBs surmised by AD18. The point at which, according to our simulation, the disk would form, is in good agreement with the estimates shown in Fig. 2, in particular the one marked by the blue asterisk.

The potential for a collapsar-driven GRB is particularly high for model **16TI**. Accreting rapidly rotating gas which adds centrifugal support, the PNS grows past the maximum mass for a non-rotating, cold PNS. During an intermittent phase, a shell with super-Keplerian rotation falling onto the PNS forms a geometrically and optically thick torus around

the PNS, inside of which neutrino emission reduces the electron fraction and the entropy. After a few 100 ms, the accretion of gas with lower angular momentum crushes the torus. The rotational profile of the star makes it likely that at a later time, around or briefly after the formation of a BH, a torus of similar characteristics will and allow for collapsar activity.

Based on very rough estimates of the possible amount of Ni synthesized in the events, we suggest that the magnetorotational explosions lead to brighter SNe. Whether or not SLSNe might be achievable due to the decay of Ni or due to the interaction with the circumstellar medium is beyond this work. The current study supports the possibility of generating SLSNe and GRBs both in the PM and the collapsar scenario from rapidly rotating and strongly magnetized Wolf-Rayet stars resulting from a CHE.

7 ACKNOWLEDGEMENTS

This work has been supported by the Spanish Ministry of Science, Education and Universities (PGC2018-095984-B-I00) and the Valencian Community (PROMETEU/2019/071). We furthermore thank for support from the COST Actions PHAROS CA16214 and GWverse CA16104. MO acknowledges support from the European Research Council under grant EUROPIUM-667912, and from the the Deutsche Forschungsgemeinschaft (DFG, German Research Foundation) - Projektnummer 279384907 - SFB 1245 as well as from the Spanish Ministry of Science via the Ramón y Cajal programme (RYC2018-024938-I). The authors thankfully acknowledge the computer resources and the technical support provided by grants AECT-2018-3-0010, AECT-2019-1-0009, AECT-2020-3-0005, and AECT-2021-1-0004 of the Spanish Supercomputing Network on cluster MareNostrum of the Barcelona Supercomputing Centre - Centro Nacional de Supercomputación, on clusters Tirant and Lluisvives of the Servei d'Informàtica of the University of Valencia (financed by the FEDER funds for Scientific Infrastructures; IDIFEDER-2018-063).

DATA AVAILABILITY

The data underlying this article will be shared on reasonable request to the corresponding authors.

REFERENCES

- Aguilera-Dena D. R., Langer N., Antoniadis J., Müller B., 2020, *The Astrophysical Journal*, 901, 114
- Aguilera-Dena D. R., Langer N., Moriya T. J., Schootemeijer A., 2018, *ApJ*, 858, 115
- Aloy M. A., Cuesta-Martínez C., Obergaulinger M., 2018, *Monthly Notices of the Royal Astronomical Society*, 478, 3576
- Aloy M. Á., Obergaulinger M., 2021, *Monthly Notices of the Royal Astronomical Society*, 500, 4365
- Antoniadis J., Tauris T. M., Ozel F., Barr E., Champion D. J., Freire P. C. C., 2016, *arXiv e-prints*, p. arXiv:1605.01665
- Blondin J. M., Shaw S., 2007, *ApJ*, 656, 366

Bugli M., Guilet J., Obergaulinger M., Cerdá-Durán P., Aloy M. A., 2020, Monthly Notices of the Royal Astronomical Society, 492, 58

Corsi A., Lazzati D., 2021, New Astronomy Reviews, 92, 101614

Drout M. R., Soderberg A. M., Gal-Yam A., Cenko S. B., Fox D. B., Leonard D. C., Sand D. J., Moon D.-S., Arcavi I., Green Y., 2011, ApJ, 741, 97

Endeve E., Cardall C. Y., Budiardja R. D., Beck S. W., Bejnood A., Toedte R. J., Mezzacappa A., Blondin J. M., 2012, ApJ, 751, 26

Endeve E., Cardall C. Y., Mezzacappa A., 2012, ArXiv e-prints

Ertl T., Janka H.-T., Woosley S. E., Sukhbold T., Ugliano M., 2016, ApJ, 818, 124

Fernández R., 2010, ApJ, 725, 1563

Gal-Yam A., 2012, Science, 337, 927

Hayakawa T., Maeda K., 2018, ApJ, 854, 43

Heger A., Woosley S. E., Spruit H. C., 2005, ApJ, 626, 350

Inserra C., 2019, Nature Astronomy, 3, 697

Iwamoto K., Mazzali P. A., Nomoto K. e. a., 1998, Nature, 395, 672

Janka H.-T., 2012, Annual Review of Nuclear and Particle Science, 62, 407

Just O., Goriely S., Janka H.-T., Nagataki S., Bauswein A., 2021, arXiv e-prints, p. arXiv:2102.08387

Just O., Obergaulinger M., Janka H.-T., 2015, MNRAS, 453, 3386

Kasen D., Bildsten L., 2010, ApJ, 717, 245

Kohri K., Narayan R., Piran T., 2005, ApJ, 629, 341

Kumar P., Narayan R., Johnson J. L., 2008, MNRAS, 388, 1729

Lazzati D., Morsony B. J., Begelman M. C., 2009, The Astrophysical Journal, 700, L47

Lazzati D., Morsony B. J., Blackwell C. H., Begelman M. C., 2012, ApJ, 750, 68

Lyman J. D., Bersier D., James P. A., Mazzali P. A., Eldridge J. J., Fraser M., Pian E., 2016, MNRAS, 457, 328

MacFadyen A. I., Woosley S. E., Heger A., 2001, ApJ, 550, 410

Maeda K., Tominaga N., 2009, MNRAS, 394, 1317

Marek A., Dimmelmeier H., Janka H.-T., Müller E., Buras R., 2006, A&A, 445, 273

Metzger B. D., Giannios D., Thompson T. A., Bucciantini N., Quataert E., 2011, MNRAS, 413, 2031

Moriya T. J., Sorokina E. I., Chevalier R. A., 2018, Space Sci. Rev., 214, 59

Mösta P., Ott C. D., Radice D., Roberts L. F., Schnetter E., Haas R., 2015, Nature, 528, 376

Mösta P., Richers S., Ott C. D., Haas R., Piro A. L., Boyd-stun K., Abdikamalov E., Reisswig C., Schnetter E., 2014, ApJ, 785, L29

Müller B., Heger A., Liptai D., Cameron J. B., 2016, MNRAS, 460, 742

Nicholl M., Guillochon J., Berger E., 2017, ApJ, 850, 55

Obergaulinger M., Aloy M. Á., 2017, MNRAS, 469, L43

Obergaulinger M., Aloy M. Á., 2020, MNRAS, 492, 4613

Obergaulinger M., Aloy M. Á., 2021, MNRAS, 503, 4942

Obergaulinger M., Janka H.-T., Aloy M. A., 2014, MNRAS, 445, 3169

O'Connor E., Ott C. D., 2011, ApJ, 730, 70

Ott C. D., Ou S., Tohline J. E., Burrows A., 2005, ApJ, 625, L119

Paxton B., Bildsten L., Dotter A., Herwig F., Lesaffre P., Timmes F., 2011, The Astrophysical Journal Supplement Series, 192, 3

Paxton B., Cantiello M., Arras P., Bildsten L., Brown E. F., Dotter A., Mankovich C., Montgomery M. H., Stello D., Timmes F. X., Townsend R., 2013, The Astrophysical Journal Supplement Series, 208, 4

Paxton B., Marchant P., Schwab J., Bauer E. B., Bildsten L., Cantiello M., Dessart L., Farmer R., Hu H., Langer N., Townsend R. H. D., Townsley D. M., Timmes F. X., 2015, The Astrophysical Journal Supplement Series, 220, 15

Paxton B., Schwab J., Bauer E. B., Bildsten L., Blinnikov S., Duffell P., Farmer R., Goldberg J. A., Marchant P., Sorokina E., Thoul A., Townsend R. H. D., Timmes F. X., 2018, The Astrophysical Journal Supplement Series, 234, 34

Rampp M., Janka H.-T., 2002, A&A, 396, 361

Reichert M., Obergaulinger M., Eichler M., Aloy M. Á., Arcones A., 2021, Monthly Notices of the Royal Astronomical Society, 501, 5733

Spruit H. C., 2002, A&A, 381, 923

Steiner A. W., Hempel M., Fischer T., 2013, ApJ, 774, 17

Surman R., McLaughlin G. C., Sabbatino N., 2011, ApJ, 743, 155

Woosley S. E., 2010, ApJ, 719, L204

Woosley S. E., Heger A., 2006, ApJ, 637, 914

Woosley S. E., Weaver T. A., 1995, ApJS, 101, 181

This paper has been typeset from a `TeX/ LATEX` file prepared by the author.